How to cite this article
Research Article

Image denoising via a new hybrid TGV model based on Shannon interpolation

E. Tavakkol, S.M. Hosseini* and A. Hosseini

Abstract

A new hybrid variational model is presented for image denoising, which incorporates the merits of Shannon interpolation, total generalized variation (TGV) regularization, and a symmetrized derivative regularization term based on l^1-norm. In this model, the regularization term is a combination of a TGV functional and the symmetrized derivative regularization term, while the data fidelity term is characterized by the l^2-norm. Unlike most variational models that are discretized using a finite-difference scheme, our approach in structure is based on Shannon interpolation. Quantitative and qualitative assessments of the new model indicate its effectiveness in restoration accuracy and staircase effect suppression. Numerical experiments are carried out using the primal-dual algorithm. Numerous real-world examples are conducted to confirm that the newly proposed method outperforms several current state-of-the-art numerical methods in terms of the peak signal to noise ratio and the structural similarity (SSIM) index.

* Corresponding author

Received 6 August 2021; revised 8 January 2022; accepted 16 January 2022

Elaheh Tavakkol
Department of Applied Mathematics, Tarbiat Modares University, P.O. Box 14115-175, Tehran, Iran. e-mail: e.tavakkol@modares.ac.ir

Seyed Mohammad Hosseini
Department of Applied Mathematics, Tarbiat Modares University, P.O. Box 14115-175, Tehran, Iran. e-mail: hossei_m@modares.ac.ir

Alireza Hosseini
School of Mathematics, Statistics and Computer Science, College of Science, University of Tehran, P. O. Box 14155-6455, Tehran, Iran. e-mail: hosseini.alireza@ut.ac.ir

1 Introduction

Image processing is an extensively utilized and rapidly growing area in computer science enriched with various applications, including image restoration [4], medical visualization [7], industrial inspection [27], law enforcement [50], and so on. Recently, various techniques have been proposed in image processing, which aims to recover the underlying true image from its degraded observation, including image denoising models [19, 49, 40, 47], image deblurring models [22, 17], image inpainting models [38, 15], image deconvolution models [28, 2], and so on. Image denoising is one of the most fundamental problems in image processing and computer vision. In the past few decades, many image denoising models have been introduced in the literature, such as variational models [39, 45], wavelet transform based models [32], nonlocal means filters [48], curvelet transform based models [29], bilateral filters [3], and so on. Variational models have been widely used in image denoising due to their capability in image feature preservation [33, 21, 43, 42, 44]. TV regularization proposed by Rudin, Osher, and Fatemi [30] (the ROF model) is a successful example of variational models. Many different papers have reported the efficiency of TV regularization [37, 13, 8, 9, 36, 18, 46]. Assume that $\Gamma \subset \mathbb{R}^d$ is a continuous domain and that $s : \Gamma \to \mathbb{R}$ is a d-dimensional image in continuous domain Γ. The continuous TV semi-norm of s is defined as

$$\text{TV}(s) = \sup \left\{ \int_\Gamma s \, \text{div} \upsilon \, d\mathbf{x} \; \Big| \; \upsilon \in C_c^1(\Gamma, \mathbb{R}^d), \; ||\upsilon||_\infty \leq 1 \right\} = \int_\Gamma |Ds| \, d\mathbf{x},$$

where $|\cdot|$ is the Euclidean norm and $|Ds|$ denotes the variation-measure of the distributional derivative Ds, which is a vector-valued Radon measure. For smooth function s, we have $Ds = \nabla s$. Therefore, TV is the integral of its gradient magnitude:

$$\text{TV}(s) = \int_\Gamma |\nabla s| \, d\mathbf{x}.$$

In TV regularization, the space of functions of bounded variation (BV) is considered as an appropriate class for image restoration. The TV semi-norm defines the norm $||s||_{\text{BV}} := ||s||_{L^1} + \text{TV}(s)$ on the space of BV functions. Although TV regularization-based techniques have become one of the most widely used regularizers due to their edge-preserving ability, they leave some form of staircase artefacts in the smooth regions of the image. To alleviate the staircase effect, several high-order methods have been proposed in the literature [12, 34, 14, 35, 25]. One technique to overcome this drawback is total generalized variation (TGV) regularization [5]. In most algorithms, the TV and TGV regularizations are discretized using a finite-differences scheme. For this reason, denoised images produced by these approaches cannot be efficiently interpolated using standard interpolation models. Several types of

research have been conducted as a remedy to this drawback [24, 26]. Shannon interpolation has been recently utilized in [1] for total variation-based image restoration leading to image improvements in terms of restoration accuracy.

In the present work, a new hybrid total generalized variation model is studied for image denoising in which the regularization term is considered to be a combination of TGV regularization and a symmetrized derivative regularization term based on l^1-norm, and the data fidelity term is characterized by the l^2-norm. Furthermore, in our approach, Shannon interpolation is used rather than a finite-differences scheme yielding efficient images in terms of restoration accuracy. Quantitative and qualitative evaluations indicate that the proposed method significantly outperforms several current state-of-the-art methods in staircase effect suppression and restoration accuracy. We employ the primal-dual algorithm presented in [11] to provide a global minimizer to the new proposed variational model.

The outline of the paper is organized as follows. In Section 2, we present the necessary definitions and basic properties of TGV model and Shannon interpolation. In Section 3, our proposed method and some necessary analytical discussions are presented. Section 4 contains the numerical algorithm. In Section 5, we present the convergence analysis for the proposed model. Section 4 is devoted to numerical experiments. Finally, Section 7 contains some concluding remarks.

2 Preliminaries

In this section, we first introduce some notations used throughout this paper, and then we briefly review the concepts of TGV regularization [5] and Shannon interpolation [1].

2.1 Notations

1. $\Omega = I_{N_1} \times I_{N_2}$ is a discrete domain of size $N_1 \times N_2$, where

$$I_{N_1} = \{0, 1, 2, \ldots, N_1 - 1\}, \quad I_{N_2} = \{0, 1, 2, \ldots, N_2 - 1\}.$$

2. $u \in \mathbb{R}^\Omega$ is a discrete gray-level image with size $N_1 \times N_2$.
3. For $d \geq 1$, $\Gamma \subset \mathbb{R}^d$ is a continuous domain.
4. $L^1_{loc}(\Gamma)$ is the set of locally Lipschitz integrable functions $s : \Gamma \to \mathbb{R}$.
5. λ_0 and λ_1 are fixed positive parameters.
6. $\mathrm{Sym}^2(\mathbb{R}^d)$ is the vector space of symmetric 2-tensors defined by

$$\mathrm{Sym}^2(\mathbb{R}^d) = \left\{ \eta : \mathbb{R}^d \times \mathbb{R}^d \to \mathbb{R} \ \middle| \ \eta \ is \ 2\text{-}linear \ and \ symmetric \right\}.$$

7. $C_c^2(\Gamma, \mathrm{Sym}^2(\mathbb{R}^d))$ is the space of 2-times continuous differentiable functions with compact support from Γ to $\mathrm{Sym}^2(\mathbb{R}^d)$.

8. $C_c^2([0, N_1] \times [0, N_2], \mathrm{Sym}^2(\mathbb{R}^2))$ is the space of 2-times continuously differentiable functions with compact support from $[0, N_1] \times [0, N_2]$ to $\mathrm{Sym}^2(\mathbb{R}^2)$.

2.2 TGV regularization and Shannon interpolation

For $s \in L^1_{loc}(\Gamma)$, the TGV functional of order 2 with weight λ is defined as [5]

$$\mathrm{TGV}^{2,\lambda}(s) = \sup \left\{ \int_{\Gamma} s \,\mathrm{div}^2 v \, d\mathbf{x} \,\Big|\, v \in C_c^2(\Gamma, \mathrm{Sym}^2(\mathbb{R}^d)), \, ||v||_\infty \le \lambda_0, \right.$$

$$\left. ||\mathrm{div} v||_\infty \le \lambda_1 \right\}, \quad (1)$$

where $\lambda = (\lambda_0, \lambda_1)$, $(\mathrm{div} v)_i = \sum_{j=1}^{d} \dfrac{\partial v_{ij}}{\partial x_j}$, and $\mathrm{div}^2 v = \sum_{i=1}^{d} \dfrac{\partial^2 v_{ii}}{\partial x_i^2} + \sum_{i<j} 2 \dfrac{\partial^2 v_{ij}}{\partial x_i \partial x_j}$.

Moreover, the infinity norms of v and the vector field w, where $w = \mathrm{div} v$, are defined as

$$||v||_\infty = \sup \left\{ \Big(\sum_{i=1}^{d} |v_{ii}(\mathbf{x})|^2 + 2 \sum_{i<j} |v_{ij}(\mathbf{x})|^2 \Big)^{1/2} \,\Big|\, \mathbf{x} \in \Gamma \right\},$$

$$||w||_\infty = \sup \left\{ \Big(\sum_{i=1}^{d} |w_i(\mathbf{x})|^2 \Big)^{1/2} \,\Big|\, \mathbf{x} \in \Gamma \right\}.$$

In second-order TGV regularization model, the space of bounded generalized variation functions of order 2, defined as

$$\mathrm{BGV}^{2,\lambda}(\Gamma) = \left\{ s \in L^1(\Gamma) \,\Big|\, \mathrm{TGV}^{2,\lambda}(s) < \infty \right\},$$

is considered as an appropriate class for image restoration. The Fenchel dual formulation of (2) for $d = 2$ and $u \in \mathbb{R}^{N_1 \times N_2}$ can be written as [6, 20]

$$\mathrm{TGV}^{2,\lambda}(u) = \min_{p \in (\mathbb{R}^2)^{N_1 \times N_2}} \lambda_0 ||\xi(p)||_1 + \lambda_1 ||\nabla u - p||_1, \quad (2)$$

where ∇u and $\xi(p)$ stand for the gradient and symmetrized derivative operators, respectively, which can be formulated as

$$\nabla u = [\partial_x^+ u \;\; \partial_y^+ u]^T, \quad \xi(p) = \begin{bmatrix} \partial_x^- p_1 & \frac{1}{2}(\partial_x^- p_2 + \partial_y^- p_1) \\ \frac{1}{2}(\partial_x^- p_2 + \partial_y^- p_1) & \partial_y^- p_2 \end{bmatrix},$$

where $(\partial_x^+ u)(i,j) = u(i+1,j) - u(i,j)$, $(\partial_y^+ u)(i,j) = u(i,j+1) - u(i,j)$,

$(\partial_x^- p_1)(i,j) = p_1(i,j) - p_1(i-1,j)$, and $(\partial_y^- p_1)(i,j) = p_1(i,j) - p_1(i,j-1)$ $((\partial_x^- p_2)(i,j)$ and $(\partial_y^- p_2)(i,j)$ can be formulated similarly) are discrete first-order derivatives [5].

The Shannon interpolate $U : \mathbb{R}^2 \to \mathbb{R}$ of the discrete image u is defined as [1]

$$U(x,y) = \frac{1}{N_1 N_2} \sum_{\alpha=-\frac{N_1}{2}}^{\frac{N_1}{2}} \sum_{\beta=-\frac{N_2}{2}}^{\frac{N_2}{2}} \varepsilon_{N_1}(\alpha) \, \varepsilon_{N_2}(\beta) \, \widehat{u}(\alpha,\beta) \, e^{2\pi i(\frac{\alpha x}{N_1} + \frac{\beta y}{N_2})}, \quad (3)$$

where $\widehat{u}(\alpha,\beta) = \sum_{k=0}^{N_1-1} \sum_{l=0}^{N_2-1} u(k,l) \, e^{-2\pi i(\frac{\alpha k}{N_1} + \frac{\beta l}{N_2})}$ is the 2-dimensional discrete Fourier transform (DFT) of u, and $\varepsilon_{N_1}(\alpha)$ and $\varepsilon_{N_2}(\beta)$ are the weighting terms [1] formulated as

$$\varepsilon_{N_1}(\alpha) = \begin{cases} 1/2 & \text{if } |\alpha| = \frac{N_1}{2}, \\ 1 & \text{otherwise,} \end{cases} \qquad \varepsilon_{N_2}(\beta) = \begin{cases} 1/2 & \text{if } |\beta| = \frac{N_2}{2}, \\ 1 & \text{otherwise.} \end{cases}$$

3 Proposed model

Let $U : \mathbb{R}^2 \to \mathbb{R}$ be the Shannon interpolate of $u \in \mathbb{R}^\Omega$ defined in (7). For the case $d = 2$ in (2), we define the second-order Shannon interpolation based TGV regularization with weight λ as

$$\text{STGV}_\infty^{2,\lambda}(u) = \sup \left\{ \int_{[0,N_1] \times [0,N_2]} U(x,y) \, \text{div}^2 V(x,y) \, dxdy \, \Big| \, V \in \right.$$

$$\left. C_c^2([0,N_1] \times [0,N_2], \text{Sym}^2(\mathbb{R}^2)), \, ||V||_\infty \le \lambda_0, \, ||\text{div}V||_\infty \le \lambda_1 \right\}, \quad (4)$$

where $\lambda = (\lambda_0, \lambda_1)$. The integral in (4) is generally difficult to compute but it can be easily approximated using the Riemann sum as

$$\text{STGV}_n^{2,\lambda}(u) = \max \left\{ \frac{1}{n^2} \langle U, \text{div}_n^2 \nu \rangle_{\mathbb{R}^{N_1 \times N_2}} \, \Big| \, \nu \in (\mathbb{R}^4)^{N_1 \times N_2}, ||\nu||_\infty \le \lambda_0, \right.$$

$$\left. ||\text{div}_n \nu||_\infty \le \lambda_1 \right\}, \quad (5)$$

where $n \ge 2$ in practice, div_n^2 is the discrete second-order divergence operator corresponding to the continuous operator div^2, and

$$\frac{1}{n^2} \langle U, \text{div}_n^2 \nu \rangle_{\mathbb{R}^{N_1 \times N_2}} = \frac{1}{n^2} \sum_{(k,l) \in \Omega_n} U(\frac{k}{n}, \frac{l}{n}) \, \text{div}_n^2 \nu(k,l),$$

in which $\mathrm{div}_n^2 \nu(k,l) = \mathrm{div}^2 V(\dfrac{k}{n}, \dfrac{l}{n})$ and

$$\Omega_n = I_{nN_1} \times I_{nN_2} = \{0, 1, 2, \ldots, nN_1 - 1\} \times \{0, 1, 2, \ldots, nN_2 - 1\}.$$

In order to compute $\mathrm{STGV}_n^{2,\lambda}(u)$, we need to obtain its Fenchel dual formulation. For this purpose, we first introduce the discrete gradient operator ∇_n, the discrete symmetrized gradient operator ξ_n, the discrete first-order divergence operator div_n, and the discrete second-order divergence operator div_n^2 in the following. To distinguish between the two cases $\mathrm{div}_n p$ and $\mathrm{div}_n \nu$, where $p \in (\mathbb{R}^2)^{nN_1 \times nN_2}$ and $\nu \in (\mathbb{R}^4)^{N_1 \times N_2}$, we use the notations $\nabla_n^* p := -\mathrm{div}_{1n} p$ and $\xi_n^* \nu := -\mathrm{div}_{2n} \nu$ ($*$ denotes the adjoint operator). As a result, div_n^2 in (3) will be denoted as $\mathrm{div}_{1n}(\mathrm{div}_{2n}(\nu))$ from now on.

Let $U : \mathbb{R}^2 \to \mathbb{R}$ be the Shannon interpolate of $u \in \mathbb{R}^\Omega$ defined in (7). The continuous gradient operator ∇U is formulated as $\nabla U(x,y) = [D_x(U(x,y)) \ \ D_y(U(x,y))]^T$ [5, 1] in which

$$D_x(U(x,y)) = \frac{2\pi i}{N_1 N_2} \sum_{\alpha=-\frac{N_1}{2}}^{\frac{N_1}{2}} \sum_{\beta=-\frac{N_2}{2}}^{\frac{N_2}{2}} \frac{\alpha}{N_1} \, \varepsilon_{N_1}(\alpha) \, \varepsilon_{N_2}(\beta) \, \widehat{u}(\alpha,\beta) \, e^{2\pi i(\frac{\alpha x}{N_1} + \frac{\beta y}{N_2})},$$

$$\tag{6}$$

$$D_y(U(x,y)) = \frac{2\pi i}{N_1 N_2} \sum_{\alpha=-\frac{N_1}{2}}^{\frac{N_1}{2}} \sum_{\beta=-\frac{N_2}{2}}^{\frac{N_2}{2}} \frac{\beta}{N_2} \, \varepsilon_{N_1}(\alpha) \, \varepsilon_{N_2}(\beta) \, \widehat{u}(\alpha,\beta) \, e^{2\pi i(\frac{\alpha x}{N_1} + \frac{\beta y}{N_2})}.$$

$$\tag{7}$$

For $(k,l) \in \Omega_n$, the discrete gradient operator $\nabla_n : \mathbb{R}^{N_1 \times N_2} \longrightarrow (\mathbb{R}^2)^{nN_1 \times nN_2}$ can be derived as [1]

$$\nabla_n u(k,l) = \nabla U(\frac{k}{n}, \frac{l}{n}). \tag{8}$$

For $p = [p_1 \ \ p_2]^T \in (\mathbb{R}^2)^{nN_1 \times nN_2}$ and $(k,l) \in \Omega_n$, the discrete first-order divergence operator $\mathrm{div}_{1n} : (\mathbb{R}^2)^{nN_1 \times nN_2} \longrightarrow \mathbb{R}^{N_1 \times N_2}$ is defined as

$$\mathrm{div}_{1n}(p(k,l)) = \mathrm{div}_{1n_1}(p(k,l)) + \mathrm{div}_{1n_2}(p(k,l)) \tag{9}$$

[5], where $\widehat{\mathrm{div}_{1n_1}(p)}(\alpha,\beta) = \widehat{D_x^*(p_1)}(\alpha,\beta)$ and $\widehat{\mathrm{div}_{1n_2}(p)}(\alpha,\beta) = \widehat{D_y^*(p_2)}(\alpha,\beta)$, for $(\alpha,\beta) \in \widehat{\Omega} = \widehat{I_{N_1}} \times \widehat{I_{N_2}}$, are formulated as [1]

$$\widehat{D_x^*(p_1)}(\alpha, \beta) = 2\pi i \frac{\alpha}{N_1} \begin{cases} \widehat{p_1}(\alpha, \beta) & \text{if } |\alpha| < \frac{N_1}{2}, |\beta| < \frac{N_2}{2}, \\[2mm] \frac{1}{2}(\widehat{p_1}(\alpha, \beta) - \widehat{p_1}(-\alpha, \beta)) & \text{if } \alpha = -\frac{N_1}{2}, |\beta| < \frac{N_2}{2}, \\[2mm] \frac{1}{2}(\widehat{p_1}(\alpha, \beta) + \widehat{p_1}(\alpha, -\beta)) & \text{if } |\alpha| < \frac{N_1}{2}, \beta = -\frac{N_2}{2}, \\[2mm] \frac{1}{4} \sum_{s_1=\pm 1} \sum_{s_2=\pm 1} s_1 \widehat{p_1}(s_1\alpha, s_2\beta) & \text{if } (\alpha, \beta) = (-\frac{N_1}{2}, -\frac{N_2}{2}), \end{cases} \tag{10}$$

$$\widehat{D_y^*(p_2)}(\alpha, \beta) = 2\pi i \frac{\beta}{N_2} \begin{cases} \widehat{p_2}(\alpha, \beta) & \text{if } |\alpha| < \frac{N_1}{2}, |\beta| < \frac{N_2}{2}, \\[2mm] \frac{1}{2}(\widehat{p_2}(\alpha, \beta) + \widehat{p_2}(-\alpha, \beta)) & \text{if } \alpha = -\frac{N_1}{2}, |\beta| < \frac{N_2}{2}, \\[2mm] \frac{1}{2}(\widehat{p_2}(\alpha, \beta) - \widehat{p_2}(\alpha, -\beta)) & \text{if } |\alpha| < \frac{N_1}{2}, \beta = -\frac{N_2}{2}, \\[2mm] \frac{1}{4} \sum_{s_1=\pm 1} \sum_{s_2=\pm 1} s_2 \widehat{p_2}(s_1\alpha, s_2\beta) & \text{if } (\alpha, \beta) = (-\frac{N_1}{2}, -\frac{N_2}{2}). \end{cases} \tag{11}$$

For $V = \begin{bmatrix} V_{11} & V_{12} \\ V_{12} & V_{22} \end{bmatrix} \in C_c^2([0, N_1] \times [0, N_2], \text{Sym}^2(\mathbb{R}^2))$, the first-order continuous divergence operator div_2 can be written as [5]

$$\text{div}_2 V(x, y) = \begin{bmatrix} D_x(V_{11}(x, y)) + D_y(V_{12}(x, y)) \\ D_x(V_{12}(x, y)) + D_y(V_{22}(x, y)) \end{bmatrix},$$

where D_x and D_y are defined as (6) and (7). Now, the discrete first-order divergence operator $\text{div}_{2n} : (\mathbb{R}^4)^{N_1 \times N_2} \longrightarrow (\mathbb{R}^2)^{nN_1 \times nN_2}$ can be derived as

$$\text{div}_{2n}\nu(k, l) = \text{div}_2 V(\frac{k}{n}, \frac{l}{n}), \tag{12}$$

for $\nu \in (\mathbb{R}^4)^{N_1 \times N_2}$ and $(k, l) \in \Omega_n$. For $p \in (\mathbb{R}^2)^{nN_1 \times nN_2}$ and $(\alpha, \beta) \in \widehat{\Omega} = \widehat{I_{N_1}} \times \widehat{I_{N_2}}$, the symmetrized gradient operator $\xi_n : (\mathbb{R}^2)^{nN_1 \times nN_2} \longrightarrow (\mathbb{R}^4)^{N_1 \times N_2}$ is given by [5]

$$\widehat{\xi_n(p)}(\alpha, \beta) = \begin{bmatrix} \widehat{D_x^*(p_1)}(\alpha, \beta) & \frac{1}{2}(\widehat{D_y^*(p_1)}(\alpha, \beta) + \widehat{D_x^*(p_2)}(\alpha, \beta)) \\[2mm] \frac{1}{2}(\widehat{D_y^*(p_1)}(\alpha, \beta) + \widehat{D_x^*(p_2)}(\alpha, \beta)) & \widehat{D_y^*(p_2)}(\alpha, \beta) \end{bmatrix},$$

where $\widehat{D_x^*(p_1)}, \widehat{D_x^*(p_2)}, \widehat{D_y^*(p_1)}$, and $\widehat{D_y^*(p_2)}$ are defined similar to (10) and (11). For $(k, l) \in \Omega_n$, $\xi_n p(k, l)$ is obtained by taking the inverse Fourier transform as

$$\xi_n p(k, l) = \begin{bmatrix} \xi_{n_1} p(k, l) & \xi_{n_3} p(k, l) \\ \xi_{n_3} p(k, l) & \xi_{n_2} p(k, l) \end{bmatrix}, \tag{13}$$

where $\xi_{n_1}p(k,l)$ is achieved as

$$\xi_{n_1}p(k,l) = \frac{1}{N_1 N_2} \sum_{\alpha=-\frac{N_1}{2}}^{\frac{N_1}{2}} \sum_{\beta=-\frac{N_2}{2}}^{\frac{N_2}{2}} \widehat{D_x^*(p_1)}(\alpha,\beta) \; e^{2\pi i(\frac{\alpha k}{N_1} + \frac{\beta l}{N_2})},$$

and $\xi_{n_2}p(k,l)$, $\xi_{n_3}p(k,l)$ can be formulated similarly.

The discrete functional $\text{STGV}_n^{2,\lambda}$ in (3) is equivalent to Fenchel dual formulation

$$\text{STGV}_n^{2,\lambda}(u) = \min_{p \in (\mathbb{R}^2)^{nN_1 \times nN_2}} \frac{\lambda_0}{n^2}||\xi_n(p)||_1 + \frac{\lambda_1}{n^2}||\nabla_n u - p||_1, \qquad (14)$$

where ∇_n and ξ_n are defined as (8) and (13), respectively. The analytical process for establishing this Fenchel dual formulation of (3) is exactly based on the lines of [5] and [20] (except the factor $\dfrac{1}{n^2}$ in (3) and the change on the operators). For this reason, we do not bring the proof here and we refer the reader to the mentioned references. Now, we concentrate on the new Shannon interpolation based the hybrid TGV (SHTGV) model defined as

$$\text{SHTGV}_n^{2,\lambda}(u) = \text{STGV}_n^{2,\lambda}(u) + \gamma \; ||\xi_n(\nabla_n(u))||_1,$$

where $\gamma > 0$ is a fixed positive parameter, $\text{STGV}_n^{2,\lambda}(u)$ is defined as (14), and $\xi_n(\nabla_n(u))$ can be easily formulated by substituting $\nabla_n(u)$ with p in the procedure of deriving ξ_n in (13). The concerned variational problem is established in the form

$$\min_u \; ||u - u_0||_2^2 + \text{SHTGV}_n^{2,\lambda}(u), \qquad (15)$$

where u is the desired restored image and u_0 is the observed data. According to our experience, the fixed value $\gamma = 0.01$ is suitable and does not need to be tuned. Therefore, one can say that no additional parameter is introduced with the new model.

4 Numerical algorithm

We use the primal-dual algorithm (Algorithm 1) presented in [11] to provide a minimizer of the variational problem (9). This primal-dual algorithm is particularly efficient in finding a solution to the saddle-point problem

$$\min_{x \in X} \; \max_{y \in Y} \; \langle Kx, y \rangle_Y + F(x) - G(y), \qquad (16)$$

where X and Y are Hilbert spaces, $K : X \longrightarrow Y$ is a linear and continuous mapping, and $F : X \longrightarrow (-\infty, \infty]$ and $G : Y \longrightarrow (-\infty, \infty]$ are proper, convex, and lower semi-continuous functionals. In order to adapt the optimization problem (9) to Algorithm 1, we need the corresponding saddle-point

Algorithm 1 The first-order primal-dual algorithm presented in [11].

1. Set $k = 0$, choose the initial estimates $x^0 \in X$, $y^0 \in Y$, $\bar{x}^0 = x^0$, and positive parameters τ and σ such that $\sigma\tau|||K|||^2 < 1$ ($||| \cdot |||$ denotes the induced l^2-norm).
2. Calculate x^{k+1}, y^{k+1}, and $\bar{x}^{k+1}$ using the following equations:
$y^{k+1} = (I + \sigma \ \partial G)^{-1}(y^k + \sigma \ K \ \bar{x}^k),$
$x^{k+1} = (I + \tau \ \partial F)^{-1}(x^k - \tau \ K^* \ y^{k+1}),$
$\bar{x}^{k+1} = 2x^{k+1} - x^k.$
3. Stop or set $k = k + 1$ and go back to step 2.

structure of this optimization problem, which is formulated as (see for details)

$$\min_{\substack{u \in \mathbb{R}^{N_1 \times N_2} \\ p \in (\mathbb{R}^2)^{nN_1 \times nN_2}}} \max_{\substack{w \in (\mathbb{R}^2)^{nN_1 \times nN_2} \\ \nu \in (\mathbb{R}^4)^{N_1 \times N_2} \\ q \in (\mathbb{R}^4)^{N_1 \times N_2}}} ||u - u_0||_2^2 + \frac{\lambda_1}{n^2}\langle \nabla_n u - p, w \rangle + \frac{\lambda_0}{n^2}\langle \xi_n(p), \nu \rangle$$

$$+ \gamma\langle \xi_n(\nabla_n u), q \rangle - I_{\{||\cdot||_\infty \leq 1\}}(w) - I_{\{||\cdot||_\infty \leq 1\}}(\nu) - I_{\{||\cdot||_\infty \leq 1\}}(q). \tag{17}$$

Using the saddle-point structure (17), x, y, the functionals F and G, and the mapping K in saddle-point problem (16) are obtained as

$$x = (u, p), \quad y = (w, \nu, q), \quad F(x) = F(u, p) = ||u - u_0||_2^2,$$

$$G(y) = G(w, \nu, q) = I_{\{||\cdot||_\infty \leq 1\}}(w) + I_{\{||\cdot||_\infty \leq 1\}}(\nu) + I_{\{||\cdot||_\infty \leq 1\}}(q),$$

$$K = \begin{bmatrix} \frac{\lambda_1}{n^2}\nabla_n & -\frac{\lambda_1}{n^2}I \\ 0 & \frac{\lambda_0}{n^2}\xi_n \\ \gamma\xi_n\nabla_n & 0 \end{bmatrix}$$

From [1, Proposition 7], we have $|||\nabla_n||| \leq n\pi\sqrt{2}$. Moreover, some computations yield $|||\xi_n||| \leq n\pi\sqrt{2}$. Therefore, an upper bound for the induced l^2-norm of K can be easily achieved as

$$|||K|||^2 < \frac{2\pi^2((\frac{\lambda_1}{n^2})^2 + (\frac{\lambda_0}{n^2})^2)n^2 + 4\pi^4\gamma^2 n^4 + (\frac{\lambda_1}{n^2})^2}{2}$$

$$+ \Big(\frac{(2\pi^2((\frac{\lambda_1}{n^2})^2 + (\frac{\lambda_0}{n^2})^2)n^2 + 4\pi^4\gamma^2 n^4 + (\frac{\lambda_1}{n^2})^2)^2}{4}$$

$$+ \frac{-16\pi^4 n^4((\frac{\lambda_1}{n^2})^2(\frac{\lambda_0}{n^2})^2 + (\frac{\lambda_1}{n^2})^2\gamma^2) - 32\pi^6\gamma^2(\frac{\lambda_0}{n^2})^2 n^6}{4} \Big)^{1/2}.$$

Now the primal-dual algorithm for solving (9) can be formulated as (see [11] for more details),

$$u^{k+1} = \arg\min_{u}\{\|u - u_0\|_2^2 + \frac{\lambda_1}{n^2}\langle \nabla_n u - p, w\rangle + \gamma\langle \xi_n(\nabla_n u), q\rangle + \frac{1}{2\tau}\|u - u^k\|_2^2\}$$

$$= \frac{u^k + \tau\frac{\lambda_1}{n^2}\mathrm{div}_{1n}(w^{k+1}) - \tau\gamma\mathrm{div}_{1n}(\mathrm{div}_{2n}(q^{k+1})) + 2\tau u^0}{1 + 2\tau}, \qquad (18)$$

$$p^{k+1} = \arg\min_{p}\{\frac{\lambda_1}{n^2}\langle \nabla_n u - p, w\rangle + \frac{\lambda_0}{n^2}\langle \xi_n(p), \nu\rangle + \frac{1}{2\tau}\|p - p^k\|_2^2\}$$

$$= p^k + \tau\ (\frac{\lambda_1}{n^2}\ w^{k+1} + \frac{\lambda_0}{n^2}\mathrm{div}_{2n}(\nu^{k+1})), \qquad (19)$$

$$w^{k+1} = \arg\max_{w}\{\frac{\lambda_1}{n^2}\langle \nabla_n u - p, w\rangle - I_{\{\|\cdot\|_\infty \leq 1\}}(w) - \frac{1}{2\sigma}\|w - w^k\|_2^2\}$$

$$= P_{\lambda_1}(w^k + \sigma\frac{\lambda_1}{n^2}\ (\nabla_n \bar{u}^k - \bar{p}^k)), \qquad (20)$$

$$\nu^{k+1} = \arg\max_{\nu}\{\frac{\lambda_0}{n^2}\langle \xi_n(p), \nu\rangle - I_{\{\|\cdot\|_\infty \leq 1\}}(\nu) - \frac{1}{2\sigma}\|\nu - \nu^k\|_2^2\}$$

$$= P_{\lambda_0}(\nu^k + \sigma\frac{\lambda_0}{n^2}\ (\xi_n(\bar{p}^k))), \qquad (21)$$

$$q^{k+1} = \arg\max_{q}\{\gamma\langle \xi_n(\nabla_n u), q\rangle - I_{\{\|\cdot\|_\infty \leq 1\}}(q) - \frac{1}{2\sigma}\|q - q^k\|_2^2\}$$

$$= P_{\gamma}(q^k + \sigma\gamma\ (\xi_n(\nabla_n \bar{u}^k))), \qquad (22)$$

where

$$P_{\lambda_1}(\bar{w}) = \frac{\bar{w}}{\max(1, |\bar{w}|)}, \quad P_{\lambda_0}(\bar{\nu}) = \frac{\bar{\nu}}{\max(1, |\bar{\nu}|)}, \quad P_{\gamma}(\bar{q}) = \frac{\bar{q}}{\max(1, |\bar{q}|)},$$

and τ and σ are positive constants. Algorithms 2 is the adapted algorithm to solve (9) (see [11] for details).

Algorithm 2 The adapted algorithm for solving the SHTGV model.

---

1. Set $k = 0$, choose the initial estimates $u^0 \in \mathbb{R}^{N_1 \times N_2}$, $p^0 \in (\mathbb{R}^2)^{nN_1 \times nN_2}$, $w^0 \in (\mathbb{R}^2)^{nN_1 \times nN_2}$, $\nu^0 \in (\mathbb{R}^4)^{N_1 \times N_2}$, $q^0 \in (\mathbb{R}^4)^{N_1 \times N_2}$, $\bar{u}^0 = u^0$, $\bar{p}^0 = p^0$, and positive parameters τ, σ such that $\sigma\tau|||K|||^2 < 1$, where

$$|||K|||^2 < \frac{2\pi^2((\frac{\lambda_1}{n^2})^2+(\frac{\lambda_0}{n^2})^2)n^2+4\pi^4\gamma^2 n^4+(\frac{\lambda_1}{n^2})^2}{2}$$
$$+ \Big(\frac{(2\pi^2((\frac{\lambda_1}{n^2})^2+(\frac{\lambda_0}{n^2})^2)n^2+4\pi^4\gamma^2 n^4+(\frac{\lambda_1}{n^2})^2)^2}{4}$$
$$+ \frac{-16\pi^4 n^4((\frac{\lambda_1}{n^2})^2(\frac{\lambda_0}{n^2})^2+(\frac{\lambda_1}{n^2})^2\gamma^2)-32\pi^6\gamma^2(\frac{\lambda_0}{n^2})^2 n^6}{4}\Big)^{1/2}.$$

2. Calculate u^{k+1}, p^{k+1}, w^{k+1}, ν^{k+1}, q^{k+1}, $\bar{u}^{k+1}$, and $\bar{p}^{k+1}$ using the following equations:

$$w^{k+1} = P_{\lambda_1}(w^k + \sigma\frac{\lambda_1}{n^2}(\nabla_n\bar{u}^k - \bar{p}^k)), \text{ where } P_{\lambda_1}(\bar{w}) = \frac{\bar{w}}{\max(1,|\bar{w}|)},$$

$$\nu^{k+1} = P_{\lambda_0}(\nu^k + \sigma\frac{\lambda_0}{n^2}(\xi_n(\bar{p}^k))), \text{ where } P_{\lambda_0}(\bar{\nu}) = \frac{\bar{\nu}}{\max(1,|\bar{\nu}|)},$$

$$q^{k+1} = P_\gamma(q^k + \sigma\gamma(\xi_n(\nabla_n\bar{u}^k))), \text{ where } P_\gamma(\bar{q}) = \frac{\bar{q}}{\max(1,|\bar{q}|)},$$

$$u^{k+1} = \frac{u^k + \tau\frac{\lambda_1}{n^2}\text{div}_{1n}(w^{k+1}) - \tau\gamma\text{div}_{1n}(\text{div}_{2n}(q^{k+1})) + 2\tau u^0}{1+2\tau},$$

$$p^{k+1} = p^k + \tau(\frac{\lambda_1}{n^2}w^{k+1} + \frac{\lambda_0}{n^2}\text{div}_{2n}(\nu^{k+1})),$$

$$\bar{u}^{k+1} = 2u^{k+1} - u^k, \quad \bar{p}^{k+1} = 2p^{k+1} - p^k.$$

3. Stop or set $k = k+1$ and go back to step 2.

---

5 Convergence analysis

In this section, we establish the convergence of the primal-dual algorithm used for solving (9). Here, we only give the basic proof frameworks and do not repeat the lengthy proving process in [11]. For this purpose, we first prove the existence of the solution to the variational problem (9) through the following theorem, which proof is similar to the proof of Theorem 1 in [23].

Theorem 1. There exists a solution to optimization problem (9).

Proof. Using the compactness property of $BV(\Omega)$, for every bounded and minimizing sequence $\{u_k\}_{k\in\mathbb{N}} \subset BV(\Omega)$, there exists a subsequence $\{u_{k_i}\}_{i\in\mathbb{N}} \subset \{u_k\}_{k\in\mathbb{N}}$ converging to some $u^* \in BV(\Omega)$. According to [5], the functions $||\nabla_n u - p||_1$, $||\xi_n(p)||_1$, and $||\xi_n(\nabla_n(u))||_1$ are proper, convex, and lower semi-continuous, and the same conclusion holds for their weighted sum $SHTGV_n^{2,\lambda}(u)$. Moreover, $\{||Au_{k_i} - u_0||_2^2\}_{i\in\mathbb{N}}$ is bounded. Therefore, we yield

$$||Au^* - u_0||_2^2 + SHTGV_n^{2,\lambda}(u^*) \leq \lim_{i\to+\infty}\inf(||Au_{k_i} - u_0||_2^2 + SHTGV_n^{2,\lambda}(u_{k_i})).$$

As a result, we can conclude the existence of the solution to optimization problem (9). □

Now the convergence theorem is exhibited in the following result.

Theorem 2. For positive parameters σ and τ, where $\sigma\tau|||K|||^2 < 1$, the sequence $\{u^k, p^k, w^k, \nu^k, q^k\}$ generated by Algorithm 2 converges to a solution of (9).

Proof. Based on Theorem 1, there exists a solution to optimization problem (9). For this reason, the set of saddle-points of (17) is non-empty. According to [5], the functions $||\nabla_n u - p||_1$, $||\xi_n(p)||_1$, and $||\xi_n(\nabla_n(u))||_1$ are proper, convex, and lower semi-continuous functions. Moreover, σ and τ in Algorithm 2 satisfy $\sigma\tau|||K|||^2 < 1$. As a result, conditions (a), (b), and (c) of Theorem 1 in [11] hold. Therefore, we can conclude that Algorithm 2 is an application of the original primal-dual algorithm in [11] and converges to a solution of (9). □

6 Experimental results

We compare the experimental results of our model with the current state-of-the-art models: isotropic TV (ITV), upwind TV [10] (UTV), Condat TV [16] (CTV), TGV [5], Shannon TV [1] (STV), and the Huber variant of Shannon TV [1] (HSTV). The experiments are conducted on test images illustrated in Figure 1. All test images are corrupted by additive white Gaussian noise of standard deviations 0.18 and 0.23. All the reconstruction processes are carried out using MATLAB R2015b on a PC with AMD A10-4600M APU with Radeon(tm) HD Graphics, 2.3-GHz Inter Core processor, and 4GB of RAM under Windows 8.

As discussed in [1], in practice, choosing the oversampling factor as $n = 2$ or $n = 3$ is enough. We set the oversampling factor $n = 2$ in STV, HSTV, and the new proposed SHTGV model. For the case $n = 3$ in STV, HSTV, and the new proposed SHTGV model, we observed that the convergence speed is decreased while no remarkable change is made in comparison with the case $n = 2$.

The restoration quality is measured by the peak signal to noise ratio (PSNR) [31] and the structural similarity index measure index [41]. The best result for each comparison item is highlighted in bold type font (see Table 2). The restored results are illustrated in Figures 2, 3, 4, 5, 6, and 7. For each model and test image, the results corresponding to parameters that provide the highest PSNR value are presented here.

The results of the ITV, UTV, CTV, STV, and HSTV models obviously illustrate staircasing effect in the affine regions. Although the TGV model is capable of suppressing the staircasing artifacts, the denoised results using this approach indicate that it sometimes leads to undesired edge blurring.

Moreover, the performance of the TGV model reveals that some regions contain an obvious staircasing effect. Our proposed model not only substantially alleviates the staircasing artifacts, but also sharply preserves important image features. Moreover, the reconstructed edges and details by our model are more distinct in comparison with other variational models. For example, zoomed-in regions in Figures 2 and 3 illustrate that the UTV model leaves some small white noise particles in denoised results. The ITV model performs to some extent better than the UTV model in noise removal, but some details and edges are not well reconstructed during the denoising process. The CTV model outperforms both the UTV and ITV models in restoration accuracy and noise removal. However, the results of the ITV, UTV, and CTV models obviously suffer from the staircasing artifacts. Although the STV and HSTV models have better performance in preserving edges and details in comparison with the ITV, UTV, and CTV models, they achieve results with obvious staircasing effect, while the staircasing effect is less sharp compared with the ITV, UTV, and CTV models. The denoised results by the TGV model indicate that this regularization scheme sometimes produces denoised results with blurred edges. The denoised results using the proposed model illustrate that this new scheme is capable of eliminating the staircasing effect and preserving the edges at the same time. In fact, the ITV, UTV, CTV, STV, and HSTV models cannot compete with our model in staircasing effect suppression, as observed in the denoised results of Figure 2. TGV model is capable of eliminating the staircasing effect to some extent, but it yields denoised results with blurred edges. As a result, we can conclude that TGV model cannot compete with our model in edge preservation. The same conclusion holds for denoised results in Figures 4, 5, and 6.

The ITV, UTV, CTV, and TGV regularization models are discretized using a finite-difference scheme, while the STV, HSTV, and SHTGV models are based on the concept of Shannon interpolation. For this reason, the images generated by means of ITV, UTV, CTV, and TGV schemes cannot be efficiently interpolated using standard interpolation models. To support this claim, croppings of the restored results are magnified with factor 3 using bicubic interpolation method, which reveals that interpolating the restored results of the ITV, UTV, CTV, and TGV models yield images with unwanted artifacts, while the results of the STV, HSTV, and SHTGV models are interpolated without creating artifacts. Since the proposed model outperforms both STV and HSTV models in staircase artifacts suppression, the staircasing artifacts are remarkably alleviated in interpolated results of our model. Moreover, the edges and details in interpolated results of our model are more distinct in comparison with the STV and HSTV models.

Figure 1: The test images used in our numerical experiments. First row, from left to right: Bird, Parrot, and Lena. Second row, from left to right: Clown, MRI1, and MRI2. Third row, from left to right: MRI3, MRI4, and MRI5. Forth row, from left to right: MRI6 and MRI7.
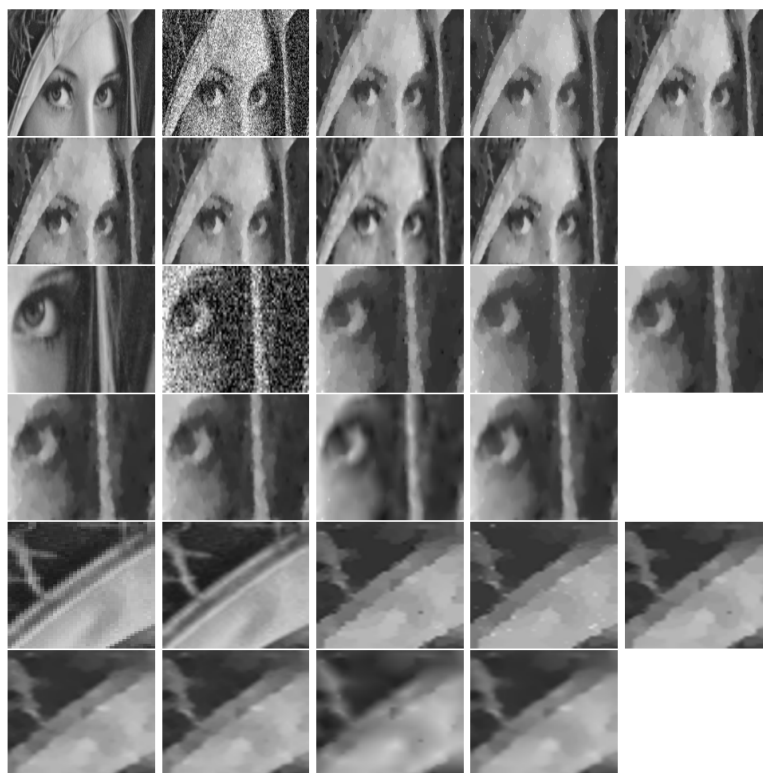
Figure 2: Performance comparison of Lena test image with additive white Gaussian noise of standard deviation 0.18. First row, from left to right: reference image, noisy image, restored results by ITV, UTV, and CTV. Second row, from left to right: restored results by STV, HSTV, TGV, and SHTGV. Images in the third and fourth rows are the corresponding zoomed-in regions of images in the first and second rows, respectively. Images in the fifth and sixth rows are croppings of the restored results of the Lena test image in the first and second rows magnified with factor 3 using the bicubic interpolation method. Fifth row, from left to right: reference image, resampling of the reference image, ITV, UTV, and CTV. Sixth row, from left to right: resampling of and STV, HSTV, TGV, and SHTGV.
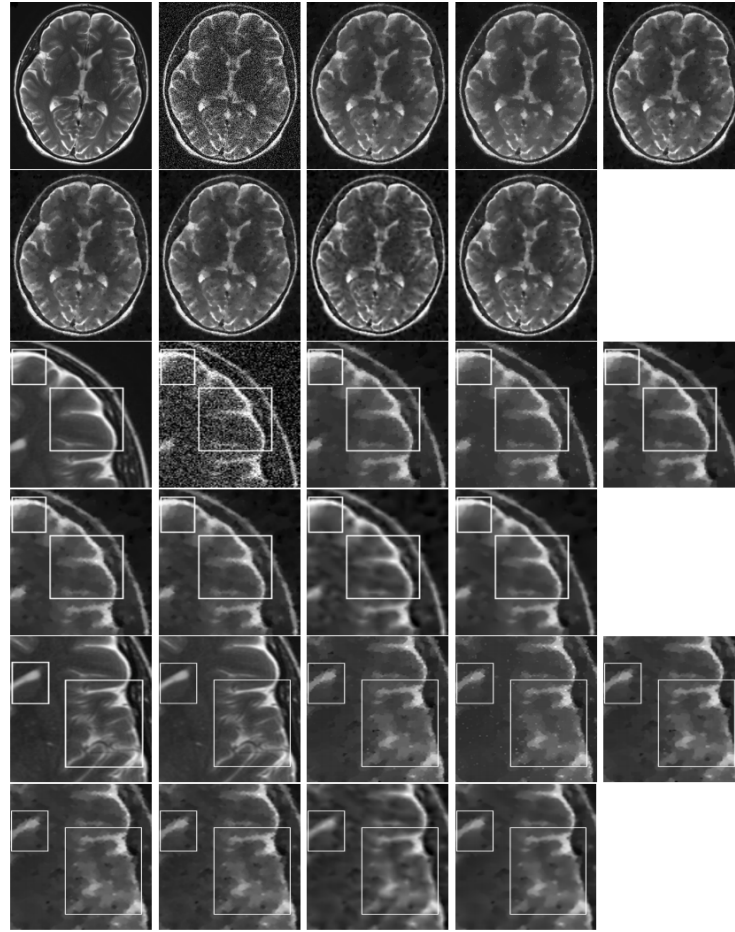
Figure 3: Performance comparison of MRI1 test image with additive white Gaussian noise of standard deviation 0.18. First row, from left to right: reference image, noisy image, restored results by ITV, UTV, and CTV. Second row, from left to right: restored results by STV, HSTV, TGV, and SHTGV. Images in the third and fourth rows are the corresponding zoomed-in regions of images in the first and second rows, respectively. Images in the fifth and sixth rows are croppings of the restored results of MRI1 test image in the first and second rows magnified with factor 3 using bicubic interpolation method. Fifth row, from left to right: reference image, resampling of the reference image, ITV, UTV, and CTV. Sixth row, from left to right: resampling of and STV, HSTV, TGV, and SHTGV.
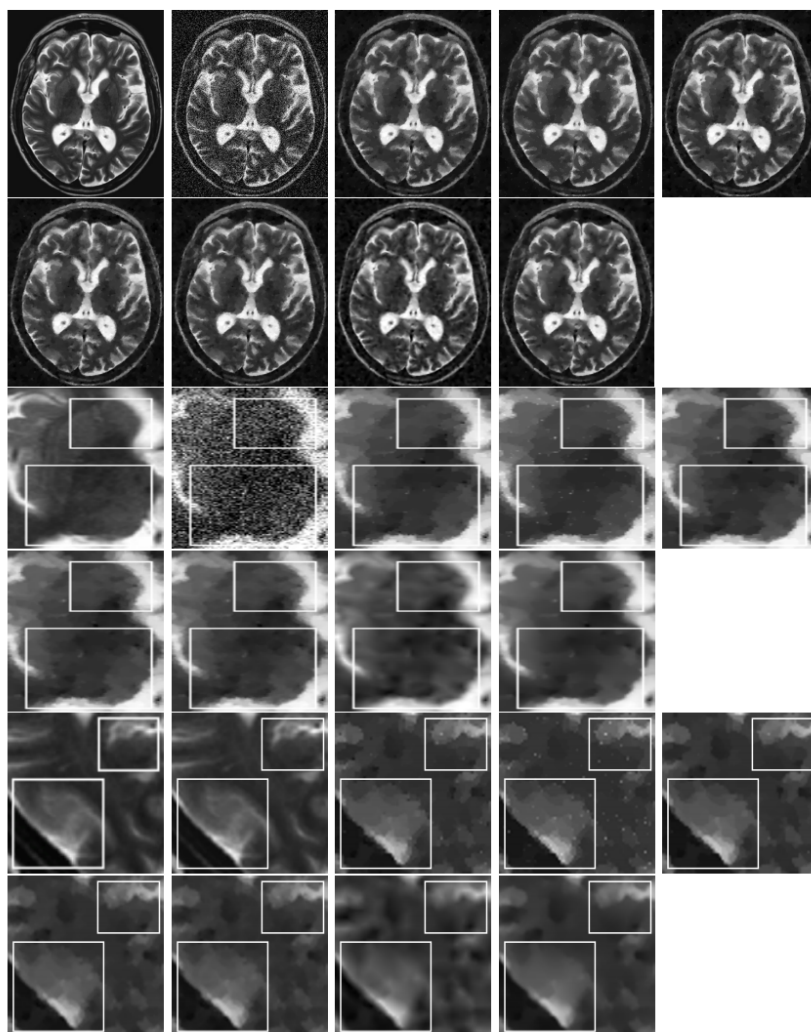
Figure 4: Performance comparison of MRI2 test image with additive white Gaussian noise of standard deviation 0.18. First row, from left to right: reference image, noisy image, restored results by ITV, UTV, and CTV. Second row, from left to right: restored results by STV, HSTV, TGV, and SHTGV. Images in the third and fourth rows are the corresponding zoomed-in regions of images in the first and second rows, respectively. Images in the fifth and sixth rows are croppings of the restored results of MRI2 test image in the first and second rows magnified with factor 3 using bicubic interpolation method. Fifth row, from left to right: reference image, resampling of the reference image, ITV, UTV, and CTV. Sixth row, from left to right: resampling of and STV, HSTV, TGV, and SHTGV.

Figure 5: Performance comparison of Bird test image with additive white Gaussian noise of standard deviation 0.18. First row, from left to right: reference image, noisy image, restored results by ITV, UTV, and CTV. Second row, from left to right: restored results by STV, HSTV, TGV, and SHTGV. Images in the third and fourth rows are the corresponding zoomed-in regions of images in the first and second rows, respectively. Images in the fifth and sixth rows are croppings of the restored results of Bird test image in the first and second rows magnified with factor 3 using bicubic interpolation method. Fifth row, from left to right: reference image, resampling of the reference image, ITV, UTV, and CTV. Sixth row, from left to right: resampling of and STV, HSTV, TGV, and SHTGV.
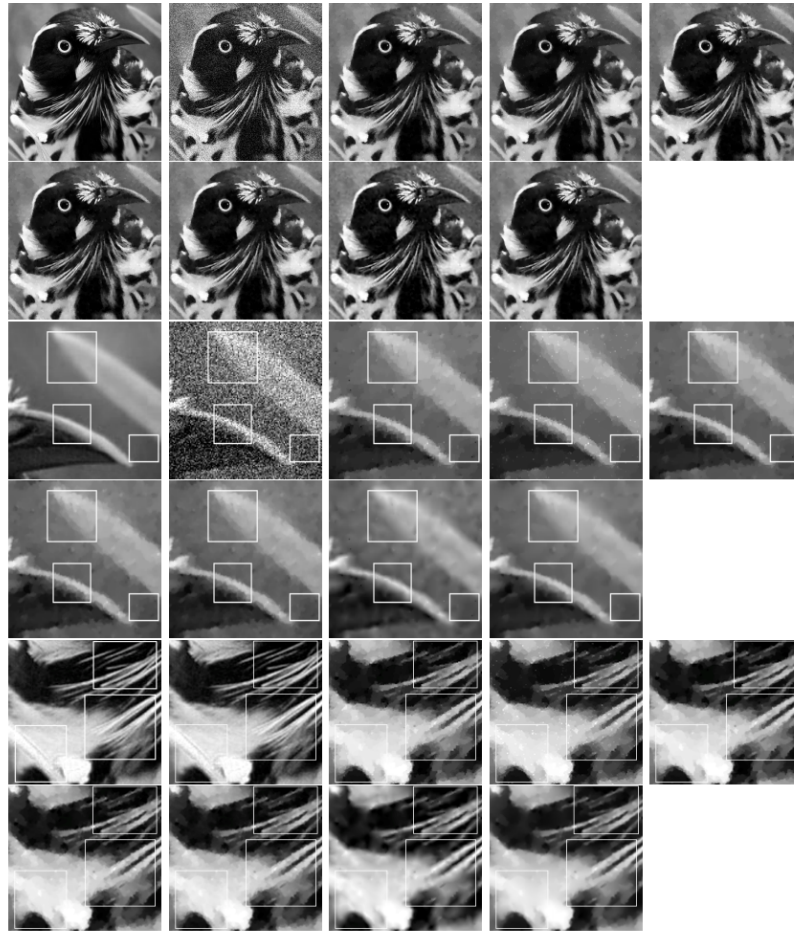
Figure 6: Performance comparison of Parrot test image with additive white Gaussian noise of standard deviation 0.18. First row, from left to right: reference image, noisy image, restored results by ITV, UTV, and CTV. Second row, from left to right: restored results by STV, HSTV, TGV, and SHTGV. Images in the third and fourth rows are the corresponding zoomed-in regions of images in the first and second rows, respectively. Images in the fifth and sixth rows are croppings of the restored results of Parrot test image in the first and second rows magnified with factor 3 using bicubic interpolation method. Fifth row, from left to right: reference image, resampling of the reference image, ITV, UTV, and CTV. Sixth row, from left to right: resampling of and STV, HSTV, TGV, and SHTGV.

Table 1: Comparison of different models in terms of PSNR and SSIM with additive white Gaussian noise of standard deviation 0.18.

Image	MRI1	MRI2
Model	PSNR / SSIM / Optimal λ	PSNR / SSIM / Optimal λ
ITV	25.30 / 0.7810 / 0.15	25.33 / 0.7687 / 0.15
UTV	24.76 / 0.7566 / 0.18	24.80 / 0.7463 / 0.18
CTV	25.64 / 0.7898 / 0.14	25.64 / 0.7792 / 0.14
STV	26.14 / 0.8113 / 0.25	26.06 / 0.7996 / 0.25
HSTV	26.07 / 0.7965 / 0.25	26.00 / 0.7936 / 0.26
TGV	26.01 / 0.7824 / $(0.4, 0.1)$	26.10 / 0.7759 / $(0.5, 0.1)$
SHTGV	**26.39** / **0.8210** / $(0.45, 0.28)$	**26.34** / **0.8139** / $(0.45, 0.28)$
Image	Bird	Parrot
Model	PSNR / SSIM / Optimal λ	PSNR / SSIM / Optimal λ
ITV	25.50 / 0.7348 / 0.15	25.33 / 0.7428 / 0.15
UTV	25.03 / 0.7109 / 0.18	24.80 / 0.7127 / 0.18
CTV	25.78 / 0.7438 / 0.14	25.63 / 0.7522 / 0.14
STV	26.09 / 0.7563 / 0.25	25.73 / 0.7464 / 0.24
HSTV	26.04 / 0.7509 / 0.26	25.68 / 0.7349 / 0.24
TGV	26.03 / 0.7416 / $(0.17, 0.11)$	25.46 / 0.7584 / $(0.15, 0.29)$
SHTGV	**26.29** / **0.7693** / $(0.45, 0.25)$	**25.84** / **0.7620** / $(0.42, 0.21)$

Table 2: Comparison of different models in terms of PSNR and SSIM with additive white Gaussian noise of standard deviation 0.23.

Image	MRI1	Parrot
Model	PSNR / SSIM / Optimal λ	PSNR / SSIM / Optimal λ
ITV	24.10 / 0.7480 / 0.2	24.17 / 0.7111 / 0.2
UTV	23.55 / 0.7053 / 0.23	23.63 / 0.6603 / 0.23
CTV	24.42 / 0.7454 / 0.18	24.46 / 0.7086 / 0.18
STV	24.90 / **0.7762** / 0.33	24.56 / 0.7146 / 0.32
HSTV	24.84 / 0.7608 / 0.33	24.51 / 0.7020 / 0.32
TGV	24.75 / 0.7439 / $(0.26, 0.14)$	24.30 / 0.7117 / $(0.19, 0.36)$
SHTGV	**25.03** / 0.7551 / $(0.5, 0.5)$	**24.62** / **0.7178** / $(0.4, 0.28)$
Image	Lena	Clown
Model	PSNR / SSIM / Optimal λ	PSNR / SSIM / Optimal λ
ITV	24.49 / 0.6701 / 0.21	22.42 / 0.6308 / 0.19
UTV	24.03 / 0.6393 / 0.25	21.97 / 0.6035 / 0.22
CTV	24.67 / 0.6759 / 0.19	22.67 / 0.6443 / 0.18
STV	24.69 / 0.6818 / 0.33	22.89 / 0.6563 / 0.31
HSTV	24.68 / 0.6814 / 0.34	22.89 / 0.6533 / 0.31
TGV	24.77 / 0.6916 / $(0.21, 0.17)$	23.00 / 0.6471 / $(0.23, 0.13)$
SHTGV	**24.83** / **0.6926** / $(0.5, 0.3)$	**23.10** / **0.6645** / $(0.6, 0.37)$

Table 3: Comparison of different models in terms of PSNR and SSIM with additive white Gaussian noise of standard deviation 0.18.

| Image	MRI3	MRI4
Model	PSNR / SSIM / Optimal λ	PSNR / SSIM / Optimal λ
ITV	24.57 / 0.7567 / 0.15	25.60 / 0.6891 / 0.15
UTV	24.06 / 0.7354 / 0.18	25.17 / 0.6676 / 0.18
CTV	24.91 / 0.7671 / 0.14	25.83 / 0.6966 / 0.14
STV	25.28 / 0.7810 / 0.25	26.16 / 0.7161 / 0.25
HSTV	25.25 / 0.7739 / 0.25	26.11 / 0.7096 / 0.26
TGV	24.99 / 0.7470 / $(0.29, 0.09)$	26.11 / 0.6988 / $(0.16, 0.12)$
SHTGV	**25.44** / **0.7893** / $(0.4, 0.2)$	**26.38** / **0.7231** / $(0.4, 0.2)$
Image	MRI5	MRI6
Model	PSNR / SSIM / Optimal λ	PSNR / SSIM / Optimal λ
ITV	25.96 / 0.6351 / 0.16	23.30 / 0.6245 / 0.14
UTV	25.50 / 0.6173 / 0.19	22.86 / 0.6057 / 0.16
CTV	26.19 / 0.6413 / 0.15	23.58 / 0.6288 / 0.13
STV	26.43 / **0.6541** / 0.26	23.89 / 0.6285 / 0.22
HSTV	26.39 / 0.6429 / 0.26	23.86 / 0.6178 / 0.22
TGV	26.22 / 0.6174 / $(0.17, 0.11)$	23.67 / 0.5766 / $(0.24, 0.08)$
SHTGV	**26.53** / 0.6444 / $(0.4, 0.2)$	**24.06** / **0.6291** / $(0.4, 0.2)$
Image	Lena	Clown
Model	PSNR / SSIM / Optimal λ	PSNR / SSIM / Optimal λ
ITV	25.45 / 0.7028 / 0.15	23.55 / 0.6866 / 0.14
UTV	25.02 / 0.6800 / 0.19	23.08 / 0.6587 / 0.16
CTV	25.67 / 0.7133 / 0.14	23.82 / 0.6979 / 0.13
STV	25.70 / 0.7189 / 0.25	23.99 / 0.7083 / 0.23
HSTV	25.69 / 0.7160 / 0.25	23.99 / 0.7053 / 0.23
TGV	25.77 / 0.7277 / $(0.17, 0.11)$	24.16 / 0.7028 / $(0.18, 0.09)$
SHTGV	**25.84** / **0.7283** / $((0.42, 0.23)$	**24.24** / **0.7149** / $(0.44, 0.25)$
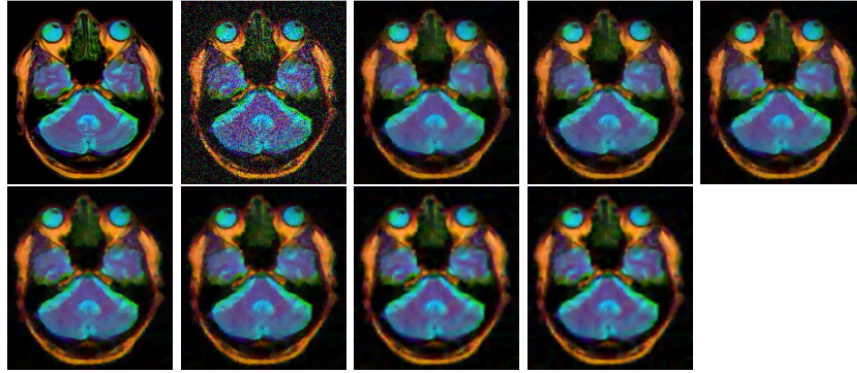
Figure 7: Performance comparison of denoised results of MRI7 with additive white Gaussian noise of standard deviation 0.18. First row, from left to right: reference image, noisy image, restored results by ITV (optimal $\lambda = 0.17$, PSNR = 25.63, SSIM = 0.7555), UTV (optimal $\lambda = 0.16$, PSNR = 25.79, SSIM = 0.7639), and CTV (optimal $\lambda = 0.17$, PSNR = 25.63, SSIM = 0.7555). Second row, from left to right: restored results by STV (optimal $\lambda = 0.26$, PSNR = 25.87, SSIM = 0.7774), HSTV (optimal $\lambda = 0.26$, PSNR = 25.81, SSIM = 0.7507), TGV (optimal $\lambda = (0.17, 0.11)$, PSNR = 25.84, SSIM = 0.7113), and SHTGV (optimal $\lambda = (0.46, 0.22)$, PSNR = 25.99, SSIM = 0.7525).

7 Conclusion

In this paper, a new hybrid TGV model was presented for image denoising. This model incorporated the advantages of Shannon interpolation, TGV regularization, and a symmetrized derivative-based l^1-norm regularized term. In comparison with some state-of-the-art techniques, experimental results illustrated that the proposed model substantially alleviates the staircasing effect and sharply preserves important image features. In fact, the reconstructed edges and details by our model were more distinct in comparison with several current state-of-the-art variational models. As we mentioned in the paper, most variational models were discretized using a finite-difference scheme, which cannot be efficiently interpolated using standard interpolation models. In this paper, we observed the efficiency of applying Shannon interpolation instead of the finite-differences schemes in the structure of variational models. Shannon interpolation applied in this paper was based on the Fourier transform. Designing a more powerful structure for Shannon interpolation based on the curvelet transform instead of Fourier transform will be considered as our future research.

References

1. Abergel, R. and Moisan, L. *The Shannon total variation*, J. Math. Imaging Vis., 59(2) (2017), 341–370.

2. Asim, M., Shamshad, F. and Ahmed, A. *Blind image deconvolution using deep generative priors*, IEEE Trans. Comput. Imaging, 6 (2020), 1493–1506.

3. Bhargava, G.U. and Gangadharan, S.V. *FPGA implementation of modified recursive box filter-based fast bilateral filter for image denoising*, Circuits, Syst. Signal Process., 40(3) (2021), 1438–1457.

4. Bioucas-Dias, J.M. and Figueiredo, M.A. *A new TwIST: Two-step iterative shrinkage/thresholding algorithms for image restoration*, IEEE Trans. Image Process., 16(12) (2007), 2992–3004.

5. Bredies, K., Kunisch, K. and Pock, T. *Total generalized variation*, SIAM J. Imaging Sci. , 3(3) (2010), 492–526.

6. Bredies, K. and Valkonen, T. *Inverse problems with second-order total generalized variation constraints*, Proceedings of SampTA, 201 (2011).

7. Burns, M., Haidacher, M., Wein, W., Viola, I. and Groller, M. E. *Feature emphasis and contextual cutaways for multimodal medical visualization*, EuroVis, 7 (2007), 275–282.

8. Caselles, V., Chambolle, A. and Novaga, M. *The discontinuity set of solutions of the TV denoising problem and some extensions*, Multiscale Model Simul. 6(3) (2007), 879–894.

9. Caselles, V., Chambolle, A. and Novaga M., *Regularity for solutions of the total variation denoising problem*, Rev. Mat. Iberoam., 27(1) (2011), 233–252.

10. Chambolle, A., Levine, S.E. and Lucier, B.J. *An upwind finite-difference method for total variation-based image smoothing*, SIAM J. Imaging Sci. 4(1) (2011), 277–299.

11. Chambolle, A. and Pock, T. *A first-order primal-dual algorithm for convex problems with applications to imaging*, J. Math. Imaging Vis., 40(1) (2011), 120–145.

12. Chan, T.F., Esedoglu, S. and Park, F.E. *Image decomposition combining staircase reduction and texture extraction*, J. Vis. Commun. Image Represent., 18(6) (2007), 464–486.

13. Chan, T.F. and Wong, C.K. *Total variation blind deconvolution*, IEEE Trans. Image Process., 7(3) (1998), 370–375.

14. Chan, T., Marquina, A. and Mulet, P. *High-order total variation-based image restoration*, SIAM J. Sci. Comput. 22(2) (2000), 503–516.

15. Chen, Y., Liu, L., Tao, J., Xia, R., Zhang, Q., Yang, K., Xiong, J. and Chen, X. *The improved image inpainting algorithm via encoder and similarity constraint*, Vis. Comput. 37(7) (2021), 1691–1705.

16. Condat, L. *Discrete total variation: New definition and minimization*, SIAM J. Imaging Sci. , 10(3) (2017), 1258–1290.

17. Dong, J. and Pan, J. *Deep outlier handling for image deblurring*, IEEE Trans. Image Process., 30 (2021), 1799–1811.

18. El Hamidi, A., Menard, M., Lugiez, M. and Ghannam, C. *Weighted and extended total variation for image restoration and decomposition*, Pattern Recognit. 43(4) (2010), 1564–1576.

19. Fang, F., Li, J., Yuan, Y., Zeng, T., Zhang, G. *Multi-level edge features guided network for image denoising*, IEEE Trans. Neural Netw. Learn. Syst., 32(9) (2021), 3956–3970.

20. Guo, W., Qin, J. and Yin, W. *A new detail-preserving regularization scheme*, SIAM J. Imaging Sci. , 7(2) (2014), 1309–1334.

21. Kang, S.H. and March, R. *Variational models for image colorization via chromaticity and brightness decomposition*, IEEE Trans. Image Process., 16(9) (2007), 2251–2261.

22. Liu, J., Yan, M. and Zeng, T. *Surface-aware blind image deblurring*, IEEE Trans. Pattern Anal. Mach. Intell., 43(3) (2021), 1041–1055.

23. Liu, X. *Total generalized variation and wavelet frame-based adaptive image restoration algorithm*, Vis. Comput. 35(12) (2019), 1883–1894.

24. Malgouyres, F. and Guichard, F. *Edge direction preserving image zooming: a mathematical and numerical analysis*, SIAM J. Numer. Anal., 39(1) (2001), 1–37.

25. Maso, G.D., Fonseca, I., Leoni, G. and Morini, M. *A higher order model for image restoration: the one-dimensional case*, SIAM J. Math. Anal., 40(6) (2009), 2351–2391.

26. Moisan, L. *How to discretize the total variation of an image?*, in the 6th International Congress on Industrial Applied Mathematics, Proceedings in Applied Mathematics and Mechanics, 7(1) (2007), 1041907–1041908.

27. Nacereddine, N., Zelmat, M., Belaifa, S.S. and Tridi, M. *Weld defect detection in industrial radiography based digital image processing*, Trans. Eng. Technol. Educ., 2 (2005), 145–148.

28. Rajora, S., Butola, M. and Khare, K. *Regularization-parameter-free optimization approach for image deconvolution*, Applied Optics. 60(19) (2021), 5669–5677.

29. Reddy, P.L. and Pawar, S. *Multispectral Image Denoising Using Curvelet Transform and Kriging Interpolation Based Wiener Filter*, Design Engineering, (2021), 838–849.

30. Rudin, L.I., Osher S. and Fatemi, E. *Nonlinear total variation based noise removal algorithms*, 'Phys. D: Nonlinear Phenom., 60(1-4) (1992), 259–268.

31. Russ JC. *The image processing handbook*, 6th ed. USA: CRC Press, 2011.

32. Sakthidasan alias Sankaran, K. and Nagarajan, V. *Noise removal through the exploration of subjective and apparent denoised patches using discrete wavelet transform*, IETE J. Res., 67(6) (2021), 843–852.

33. Samson, C., Blanc-Féraud, L., Aubert, G. and Zerubia, J. *A variational model for image classification and restoration*, IEEE Trans. Pattern Anal. Mach. Intell., 22(5) (2000), 460–472.

34. Scherzer, O. *Denoising with higher order derivatives of bounded variation and an application to parameter estimation*, Computing, 60(1) (1998), 1–27.

35. Setzer, S.I. and Steidl, G.A. *Variational methods with higher order derivatives in image processing*, Approximation, 12 (2008), 360–386.

36. Valsesia, D. and Boufounos, P. T. *Multispectral image compression using universal vector quantization*, IEEE Information Theory Workshop (ITW), (2016), 151–155.

37. Vogel, C.R. and Oman, M.E. *Fast, robust total variation-based reconstruction of noisy, blurred images*, IEEE Trans. Image Process., 7(6) (1998), 813–824.

38. Wang, N., Zhang, Y. and Zhang, L. *Dynamic selection network for image inpainting*, IEEE Trans. Image Process., 30 (2021), 1784–1798.

39. Wang, W., Zhang, C. and Ng, M.K. *Variational model for simultaneously image denoising and contrast enhancement*, Opt. Express, 28(13) (2020), 18751–18777.

40. Wang, Y., Song, X. and Chen, K. *Channel and space attention neural network for image denoising*, IEEE Signal Process. Lett., 28 (2021), 424–428.

41. Wang, Z., Bovik, A.C., Sheikh, H.R. and Simoncelli, E.P. *Image quality assessment: from error visibility to structural similarity*, IEEE Trans. Image Process., 13(4) (2004), 600–612.

42. Wu, T., Gu, X., Wang, Y. and Zeng, T. *Adaptive total variation based image segmentation with semi-proximal alternating minimization*, Signal Process. 183 (2021), 108017.

43. Wu, T. and Shao, J. *Non-convex and convex coupling image segmentation via tgpv regularization and thresholding*, Adv. Appl. Math. Mech., 12 (2020), 849–878.

44. Wu, T., Shao, J., Gu, X., Ng, M.K. and Zeng, T. *Two-stage image segmentation based on nonconvex $l_2 - l_p$ approximation and thresholding*, Appl. Math. Comput., 403 (2021), 126168.

45. Yuan, J. *An improved variational model for denoising magnetic resonance images*,Comput. Math. Appl. , 76(9) (2018), 2212–2222.

46. Yuan, Q., Zhang, L. and Shen, H. *Multiframe super-resolution employing a spatially weighted total variation model*, IEEE Trans. Circuits Syst. Video Technol., 22(3) (2011), 379–392.

47. Zhang, H., Chen, H., Yang, G. and Zhang, L. *LR-Net: Low-rank spatial-spectral network for hyperspectral image denoising*, IEEE Trans. Image Process., 30 (2021), 8743–8758.

48. Zhang, X. *Two-step non-local means method for image denoising*, Multidimens. Syst. Signal Process., (2021), 1–26.

49. Zhang, Y., Li, K., Li, K., Sun, G., Kong, Y. and Fu, Y. *Accurate and fast image denoising via attention guided scaling*, IEEE Trans. Image Process., 30 (2021), 6255–6265.

50. Zhang, Z. and Blum, R.S. *Region-based image fusion scheme for concealed weapon detection*, in Proceedings of the 31st Annual Conference on Information Sciences and Systems, (1997), 168–173.

How to cite this article